Catalysis Science & Technology

PAPER

View Article Online
View Journal

Cite this: DOI: 10.1039/c5cy02208h

Design of an MWW zeolite catalyst for linear alkylbenzene synthesis with improved catalytic stability

Hsiang-Ting Yen,[a] Jhao-Jyun Wang,[a] Siou-Huei Siao,[a] Seung Hyeok Cha,[b] Suk Bong Hong,[b] Sulaiman S. Al-Khattaf,[c] Ikai Wang[d] and Tseng-Chang Tsai*[a]

Received 18th December 2015,
Accepted 2nd February 2016

DOI: 10.1039/c5cy02208h

www.rsc.org/catalysis

The effect of micro–meso hierarchical porosity on the catalytic performance of MWW zeolites during linear alkylbenzene (LAB) synthesis was studied. The catalytic active sites of the MWW zeolite during LAB synthesis are identified as the acid sites located on the external surface cage (EC-12) and the internal supercage (C10-12). The catalytic stability of MCM-22 obtained from the optimum preparation protocol could be improved by increasing the number of EC-12 cages as well as increasing the S_{meso} and pore volume. The catalytic activity of ITQ-2 by delamination for LAB synthesis is mainly attributed to the acid site located at surface cage EC-12. The ITQ-2 sample subjected to the optimum delamination procedure exhibited very strong stability even in benzene lean LAB feed or 0.1% octadiene-containing LAB feed. Alternatively, the pillared MCM-36 zeolite increases the C10-12 supercage and mesoporous surface area, enabling MCM-36 to catalyse a lower LAB product selectivity with formation of more di-alkylate by-products with a similar LAB isomer selectivity.

Introduction

Long chain linear alkylbenzene (LAB) is one of the key intermediates in the detergent and surfactant industry. It has a generic chemical formula of $C_6H_5C_nH_{2n-1}$ with n being a number between 10 and 16. LAB is produced industrially from benzene alkylation with α-olefin or the so-called "Pacol feed" (a long chain olefin produced from *n*-paraffin dehydrogenation) by homogenous catalysis using HF or $AlCl_3$ or by heterogeneous catalysis using a clay catalyst.[1] The detergent industry has been pursuing the development of an environmentally friendly alkylation process by using a solid acid catalyst. On the other hand, among various LAB isomers, the 2-phenyl alkane (2-LAB) sulfonate is the most biodegradable. A catalytic process generating high 2-LAB isomer product selectivity is environmentally favourable.

The most studied solid acid catalysts for LAB synthesis are zeolites and some metal oxides. Whereas homogeneous catalysts such as $AlCl_3$ and HF catalyse a relatively lower LAB product selectivity with 2-LAB selectivity of around 30% and 15%, respectively,[2] and high multi-alkylation by-products, various zeolites catalyse higher LAB product selectivity with a much higher 2-LAB isomer selectivity.[3] Thus far, solid acid catalysts always suffer from serious deactivation problems with a short cycle length.[4] The fast deactivation of the solid acid catalyst is currently a major hurdle for practical applications.

The zeolite catalyst design for LAB synthesis always deals with designing parameters such as topology, crystal morphology, porosity, *etc.* It is further complicated with the effect of zeolite sample source,[5] unintended modification in mesoporosity during general practices such as post-treatments, thermal activation, chemical activation and functionalization,[6] and process conditions such as LAB feed purity, benzene/olefin ratio and reaction temperature, *etc.* While most of the 12-oxygen membered ring (12-MR) zeolites are catalytically active for LAB synthesis, the 8-MR and 10-MR zeolites are inactive.[7] Lin *et al.* have demonstrated that base-treated but not steam-treated mordenite by introducing mesoporosity exhibited the highest ever reported 2-LAB isomer selectivity up to 78% and a strong catalytic stability.[5] Zeolite beta exhibited 2-LAB selectivity of 30–45%.[8] Cao *et al.* reported that a subtle change from a circular pore mouth of 7.4 Å of faujasite (FAU) to an elliptic pore of 7.4 × 6.5 Å of the zeolite EMT resulted in a dramatic increase in 2-LAB isomer selectivity from 28% for FAU to 42% for EMT.[9]

Layer zeolites have opened up a new research area for many catalytic applications.[10] MWW zeolites including the

[a] *Department of Applied Chemistry, National University of Kaohsiung, Kaohsiung 811, Taiwan, Republic of China. E-mail: tctsai@nuk.edu.tw; Fax: +886 7 5919348; Tel: +886 7 5919457*
[b] *Center for Ordered Nanoporous Materials Synthesis, School of Environmental Science and Engineering, POSTECH, Pohang 790-784, Korea*
[c] *Center of Research Excellence in Petroleum Refining and Petrochemicals, King Fahd University of Petroleum and Minerals, Dhahran 31261, Saudi Arabia*
[d] *Department of Chemical Engineering, National Tsing-Hua University, Hsinchu 300, Taiwan, Republic of China*

MCM-22 zeolite share a common hierarchical pore structure consisting of two independent two-dimensional pore systems, including the sinusoidal channels with 10-MR openings and the large 12-MR supercages (0.71 × 0.71 × 1.81 nm) interconnected by the 10-MR windows, as well as one external isolated 12-MR cage located on the inter-crystalline surface.[11] The MCM-22 precursor could be swollen and delaminated to form layer zeolite ITQ-2 with the creation of an extraordinary mesoporous surface area.[12] MCM-36 prepared from pillaring of MCM-22 has a more open structure with enhanced adsorption capacity.[13] Their structures and properties could be altered with different swelling, delamination or pillaring procedures, making MWW zeolites even more versatile.[14–16]

MWW zeolites with hybrid micro–meso porosity could have great potential in catalysis for many catalytic reactions, such as environmentally friendly catalysis of MCM-22 for benzene isopropylation,[17] ethylation and Beckmann rearrangement reaction.[18] The acid sites associated with different environments in three pore geometries could be useful for shape selective catalysis that can provide unique shape-selective catalytic properties in several model reactions.[19] Du and Olson demonstrated by means of selective poisoning of collidine that benzene alkylation with ethylene takes place on the external surface 12-MR cage.[20] Min *et al.* reported that the active site during methanol-to-olefin reaction is located on the two-dimensional sinusoidal 10-MR channels in H-MCM-22.[21] The present paper studies the catalytic properties of MWW zeolites for LAB synthesis from the perspective of catalytic stability and product selectivity. The active sites of different MWW zeolites are experimentally identified by using collidine selective poisoning and *n*-propylbenzene disproportionation tests. The effects of feed composition, diene impurity and operating conditions are examined.

Experimental

1.1. Preparation of MCM-22 precursor

Three MCM-22 samples denoted as M22_CS, M22_AR and M22_ASp were prepared from colloidal silica, aerosol and alumina-silicate microspheres, respectively. M22_CS was prepared following the procedure reported by Tsai *et al.*,[18] from a mixture using a hexamethyleneimine (HMI) template with the molar composition of 1 SiO_2 : 0.02 Al_2O_3 : 0.1 Na_2O : 0.35 HMI : 25 H_2O. Briefly, solution A was prepared from 29.4 g of colloidal silica solution HS-40 and 9 g of water. Solution B was prepared by mixing 0.5 g of NaOH, 1.13 g of $NaAlO_2$ and 27.3 g of water. Solution B was then mixed with solution A, 5.09 g of HMI and finally 9 g of water. The mixture was capped and stirred at 600 rpm for 10 minutes. Finally, 0.16 g of MCM-22 crystal counted as 0.2% of silica source was added to the mixture for seeded crystallization under the hydrothermal conditions of 443 K for 4 days with continuous stirring at 550 rpm. A solid product, denoted as M22-P (MCM-22 precursor), was obtained by filtration of the crystallization mixture, followed by washing with water and air drying at 333 K for 6 h. (Na,H)M22 was obtained from M22-P by calcination in air at 813 K for 8 h. The H-M22 product denoted as M22 was prepared from (Na,H)M22 by ion exchange three times with NH_4Cl solution at 353 K and 8 h, followed by drying and calcination in air at 813 K for 8 h.

M22_AR with a Si/Al ratio of 16.8 was synthesized using hexamethyleneimine as an organic structure-directing agent according to the procedures described by Corma *et al.*[22] M22_ASp was kindly provided by Sinopec Research Institute of Petroleum Processing, following the patent literature.[23]

1.2. Swelling after-treatment of the MCM-22 precursor

MWW precursor M22_CS(P) was intercalated with a mixture of cetyltrimethylammonium chloride (CTMAC) and tetrapropylammonium hydroxide (TPAOH) at a molar ratio of M22_CS(P) : 4 CTMAC (25%) : 1.2 TPAOH (40%). Briefly, 1 g of M22_CS(P) was dispersed in 2.7 g of distilled water and then 14.8 g of 25% CTMAC and 4.44 g of 40% TPAOH were added. The mixture was then refluxed at 353 K for 24 h. The solution was then filtrated to obtain a solid product denoted as M22_CS(S).

1.3. Preparation of ITQ-2

A swollen MCM-22 precursor M22_CS(S) was subjected to a series of treatments for the preparation of (Na,H)IQ2_CS-*x* sequentially with ultrasonication at 323 K for *x* min, addition of 37% HCl solution until pH $<$ 2, centrifuge recovery at 20 000 rpm and water washing, drying and air calcination at 813 K for 8 h. Ultrasonication times of 10, 45 and 90 min were applied. H-IQ2_CS-*x* was prepared from (Na,H)IQ2_CS-*x* by ion exchange three times with NH_4Cl solution at 353 K and 8 h, followed by drying and calcination in air at 813 K for 8 h.

1.4. Preparation of MCM-36

M22_CS(S) was pillared with tetraethyl orthosilicate (TEOS) by refluxing the mixture of M22_CS(S)/TEOS at a ratio of 0.2 wt/wt at 353 K under nitrogen for 25 h. One gram of solid product was mixed with 20 mL of 2 M NH_4NO_3 at 353 K under nitrogen for 6 h for hydrolysis twice. The solid product was recovered and calcined and ion-exchanged to obtain M36_CS.

2. Characterization of MWW zeolites

All samples were submitted to intense ultrasonic irradiation before characterization. X-Ray diffraction patterns of the zeolite coatings were obtained using a Rigaku Multiflex model 2 kW X-ray diffractometer, with Cu Kα radiation generated at 40 kV and 30 mA. The morphology of the zeolite coating was examined using a HITACHI S-3400 N scanning electron microscope (SEM) at 15 kV operating voltage and 10 mm working distance.

Nitrogen or argon adsorption–desorption isotherms and BET (Brunauer–Emmett–Teller) surface area measurements were conducted using a Micromeritics ASAP2020 at 77 K. The samples of 0.1–0.15 g were first degassed in vacuum at a

ramp rate of 10 °C min^{-1} up to 623 K for 8 h. The BET method was used to calculate the specific surface areas. The pore volumes and pore size distributions were derived from the desorption isotherms using the Barrett–Joyner–Halenda (BJH) method.

NH_3 TPD was recorded using a flow through micro-reactor system connected to a gas chromatograph equipped with a thermal conductivity detector. A catalyst sample of 50 mg was pre-treated at 623 K in helium flowing gas for 1 h and then cooled down to 403 K. The sample was purged with NH_3 gas at 403 K for 1 h and then evacuated at 523 K to remove excess ammonia at the same temperature for 30 min. NH_3 desorption was conducted by heating the sample from 523 K to 723 K at a heating rate of 10 °C min^{-1}, and maintaining the temperature at 723 K for 1.5 h.

3. Catalytic testing

Benzene (LC grade), 1-dodecene (LC grade), *n*-decane (LC grade, Tedia) and *n*-propylbenzene (*n*-PB) were used without further purification. *n*-Decane was used as an internal reference to measure the conversion of 1-dodecene. Benzene alkylation or *n*-PB disproportionation tests were conducted in a continuous flow fixed-bed reactor. All catalyst samples crushed into particle sizes of 12–20 mesh were mixed with quartz sand particles (50–70 mesh, Sigma-Aldrich) to prevent extra-granular diffusion limitation and to improve catalyst dispersion, flow dispersion and reactor temperature homogeneity. Its catalytic performance was evaluated in the presence of hydrogen under different reaction conditions. The reactor effluent was analysed using a China Chromatography model 8700F equipped with a flame ionization detector and an OV101 packed column.

Results

1. Preparation of MCM-22

Three MCM-22 samples denoted as M22_AR, M22_CS and M22_ASp were prepared from three different silica precursors, namely, Aerosil, colloidal silica and aluminosilicate microspheres/nanoparticles, respectively. Fig. 1 depicts the XRD patterns of different MCM-22 samples confirming the MWW zeolite structure. The XRD pattern of a MCM-22 precursor denoted as M22_CS(P) was also presented for reference.

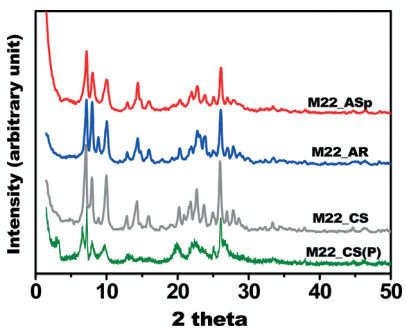

Fig. 1 X-ray diffraction patterns of the MCM-22 samples.

After calcination at 813 K, the XRD peaks of the (001) and (002) reflection planes corresponding to diffraction angles of 2θ = 3.1 and 6.6° in the M22_CS(P) sample disappeared, indicating the transformation of the two-dimensional M22_CS(P) precursor into three-dimensional M22_CS.

The three MCM-22 samples all exhibited the same powder XRD patterns in agreement with the literature data. The powder XRD pattern confirmed a typical MCM-22 framework structure exhibiting a main peak at a diffraction angle of 2θ of 25.9°. Notice that M22_AR and M22_CS exhibited a contamination diffraction peak that appeared at 2θ of 8.8°. It could be due to the presence of the MFI or FER phase.

Fig. 2 depicts the morphology of the three MCM-22 samples. All the samples exhibited a platelet morphology. M22_CS exhibited a uniform morphology in regular stacking of thin round platelets in the size of 250 nm. The morphology of M22_ASp was rather non-uniform showing agglomeration of scattered thick platelets in 200 nm size. On the other hand, M22_AR was in the size of 100 nm, apparently smaller than the other two MCM-22 samples.

The nitrogen adsorption–desorption isotherms of the different MCM-22 samples are shown in Fig. 3. The adsorption–desorption curves showed a typical type IV isotherm with an H3 hysteresis loop as an indication of the presence of mesopores. Their textural properties are depicted in Table 1. The mesoporous surface area (S_{meso}), mesoporous volume (V_{meso}) and pore size (D_p) all ranked in the order of M22_AR > M22_ASp > M22_CS. Unprecedentedly, S_{meso} was significantly affected by the morphology of the MCM-22 sample. Corma *et al.* identified the surface area of 10-MR and 12-MR pores from the Ar adsorption isotherm.[24] The argon

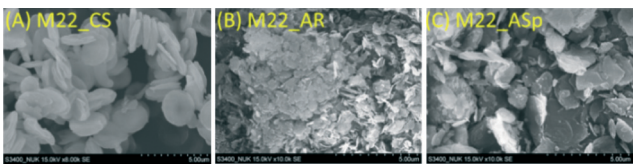

Fig. 2 The morphology of the three MCM-22 samples (A) M22_CS; (B) M22_AR; (C) M22_ASp.

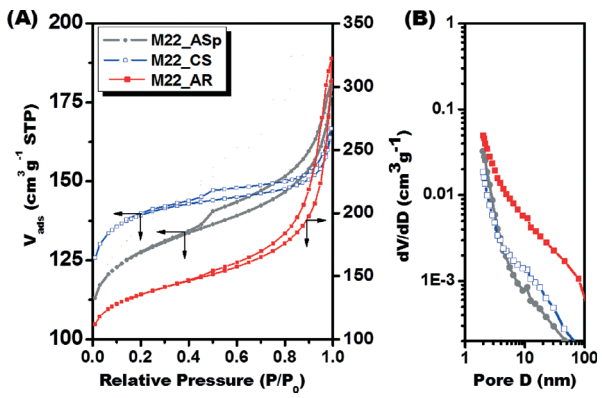

Fig. 3 (A) Nitrogen adsorption–desorption isotherms; and (B) pore size distribution of different MCM-22 samples (M22_AR, M22_ASp, and M22_CS).

Table 1 Textural properties of different MCM-22 samples, ITQ-2 samples, and MCM-36

Sample ID	SA ($cm^3\ g^{-1}$)		Pore volume ($cm^3\ g^{-1}$)		Size (nm)	TPD acidity ($\mu mol\ g^{-1}$)	
	S_{BET}	S_{meso}	V_{total}	V_{meso}	D_p	Total	Distribution[a]
M22_AR	461.5	294.6	0.50	0.36	9.5	653	600(358), 653(109), 852(208)
M22_ASp	429.7	100.9	0.27	0.12	6.9	880	644(524), 860(356)
M22_CS	467.9	79.3	0.25	0.07	4.9	737	658(499), 848(238)
IQ2_CS-10	400.5	222.5	0.48	0.40	4.9	—	—
IQ2_CS-45	556.0	320.5	0.60	0.49	6.3	—	—
IQ2_CS-90	772.9	656.3	0.78	0.73	7.8	693	603(196), 654(159), 828(338)
M36_CS	606.3	437.1	0.48	0.40	4.0	625	610(121), 773(463), 873(5)

[a] TPD temperature, K; (acid amount, $\mu mol\ g^{-1}$).

adsorption–desorption isotherms of the M22_AR sample are shown in Fig. 4. Two clear maxima of pore size distribution appeared at 0.46 and 0.63 nm representing the micropore of MWW (Fig. 4B). There was no obvious maximum peak in the mesopore range. The observation is in agreement with that reported by Roth *et al.*[13]

As will be discussed below, the higher S_{meso} value of M22_AR and the delaminated or pillared M22_AR should be attributed to the more open 12-MR external surface cage and the internal supercage rather than the inter-crystalline voidage. On the other hand, M22_ASp had the highest TPD acidity followed by M22_CS and M22_AR (Table 1). The TPD spectra of the three MCM-22 samples (Fig. 5) indicated that M22_AR had the lowest acid strength and total acidity.

2. Preparation of MWW zeolites

The layer material MCM-22(P) could be swollen, exfoliated and pillared under suitable conditions to prepare other MWW zeolites. The M22_CS(P) was subjected to swelling post-treatment for 24 h at 353 K with CTMAC–TPAOH basic solution. Fig. 6 depicts the XRD patterns of M22_CS(P) before and after swelling with CTMAC (Fig. 6 traces a and b). The swollen M22_CS(P) shows a shift in the (001) and (002) reflection peaks to lower angles after intercalation of CTMAC, indicating an increase in layer spacing, and a merger between (101) and (102) reflections. The reflection angles of the (220) and (310) planes were not affected by swelling, indicating the retention of the layer structure. These XRD data agreed with previous reports.[14]

The two-dimensional layer material ITQ-2 was prepared from the swollen M22_CS(S) material by delamination under ultrasonication in highly acidic solution at 323 K, followed by with sequential treatments subjected to recovery and air calcination. Three ITQ-2 samples, denoted as IQ2_CS-10, IQ2_CS-45, and IQ2_CS-90, were obtained by increasing the ultrasonication time for consolidating delamination. As shown in Fig. 6, the XRD pattern intensities of the ITQ-2 products were relatively weak and broad, indicating a reduction in the domain size of the crystal (traces c–e). The ITQ-2 samples prepared at increasing delamination severity exhibited corresponding decreases in the peak intensity of the (100) and (310) reflections. All of them did not show the (001) and (002) reflection peaks associated with the long-range periodicity of 2.5 nm layer spacing along the *c* axis in the MCM-22 topology, confirming the delaminated layer ITQ-2 structure (Fig. 6g).

Fig. 6f depicts the XRD pattern of the pillared MCM-36 sample denoted as M36_CS. The weak peak intensity suggests an amorphous structure. However, weak peaks appearing at the 2θ values of 1.9, 7.2, 14.5 and 26.1° corresponding to the (001), (100), (200) and (310) reflection were visible, indicating clearly the existence of the crystalline MCM-36 structure.

Fig. 7 depicts the nitrogen adsorption–desorption isotherms of MWW zeolites. The adsorption–desorption curves of the MWW zeolite samples except M36_CS showed a typical

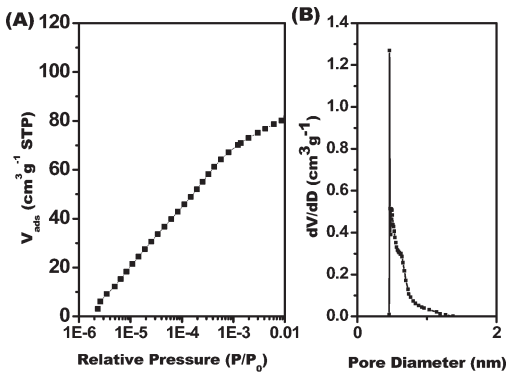

Fig. 4 (A) Argon adsorption–desorption isotherms at $P/P_0 < 0.01$; and (B) micropore size distribution of M22_CS.

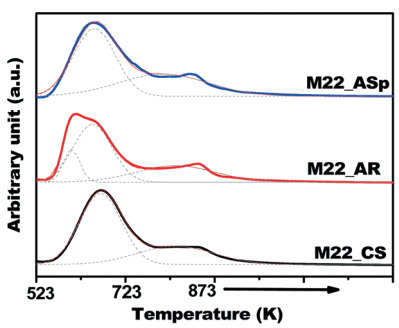

Fig. 5 Ammonia temperature programmed desorption spectra of different MCM-22 samples (M22_AR, M22_ASp, and M22_CS).

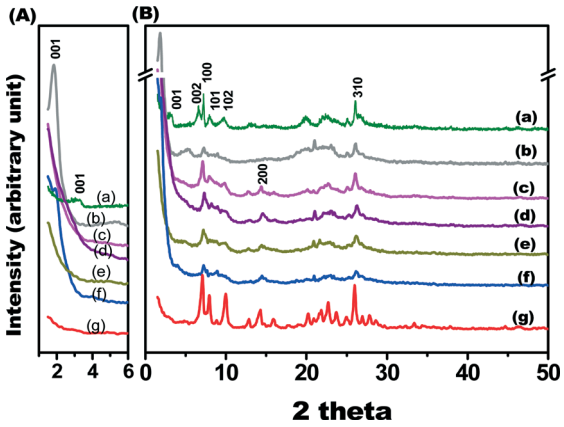

Fig. 6 (A) Small angle; and (B) wide angle XRD patterns of (a) M22_CS(P), (b) M22_CS(S), (c) IQ2_CS-10, (d) IQ2_CS-45, (e) IQ2_CS-90, (f) M36_CS, and (g) M22_CS.

type IV isotherm with an H3 hysteresis loop. Their textural properties are depicted in Table 1. All the ITQ-2 samples exhibited significantly higher S_{meso}, V_{meso} and mesopore size than the corresponding MCM-22 sample (M22_CS). They increased with increasing delamination severity, ranging from M22_CS-90 > M22_CS-45 > M22_CS-10. Unprecedentedly, IQ2_CS-10 exhibited an adsorption isotherm and textural properties similar to M22_AR.

On the other hand, M36_CS exhibited a type IV adsorption isotherm with an H4 hysteresis loop, indicating an interconnecting mesopore structure. The IQ2_CS-90 and M36_CS samples possessed a much higher S_{meso} value than all the MCM-22 samples. The high mesoporous surface area (Table 1) confirmed the pillared MWW structure. As shown in Table 1, the TPD acidities of ITQ-2 and MCM-36 were lower than that of MCM-22.

3. Characterization of 10- and 12-MR pore structures with *n*-propylbenzene (*n*-PB) disproportionation

It has been demonstrated that the reaction mechanism of alkylbenzene disproportionation changes with the pore structure of the zeolite.[25] While 12-MR zeolites catalyse the bi-molecular mechanism during *n*-PB disproportionation producing selectively *n*,*n*-di-propylbenzene (*nn*DPB) isomers, 10-MR zeolites catalyse the mono-molecular dealkylation–alkylation mechanism giving *nn*DPB and *n*-,i-(*ni*DPB) isomers in thermodynamic equilibrium composition at a 50/50 ratio. Presumably, *nn*DPB isomer selectivity during *n*-PB disproportionation could be used for gauging the active sites of the 12-MR pore and for probing the location of the active sites in MWW zeolites.

As shown in Table 2, the ITQ-2 samples and MCM-36 all catalysed higher *nn*DPB selectivity than the M22_CS. In terms of *nn*DPB isomer selectivity, the MCM-22 samples ranked in the decreasing order of M22_AR ≈ M22_ASp > M22_CS, which followed the same order of S_{meso} (Table 1). Presumably, M22_AR possessed more accessible actives sites located on the surface 12-MR cage than the other samples, and the M22_CS had the lowest active sites on the surface 12-MR cage.

Similarly, the delaminated ITQ-2 and the pillared MCM-36 all had increasing S_{meso}. Their increasing *nn*DPB isomer selectivity in reference to MCM-22 indicated that more surface 12-MR cages were generated on the MWW zeolite after delamination or pillaring, and the external active sites located on the surface 12-MR cage are catalytically active and more accessible. Among the three ITQ-2 samples, their *nn*DPB isomer selectivity ranked in the decreasing order of IQ2_CS-90 > IQ2_CS-45 > IQ2_CS-10, suggesting that increasing delamination severity could generate increasing number of 12-MR cages on the external surface.

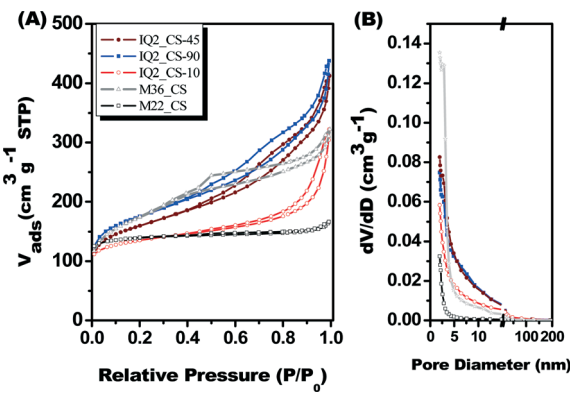

Fig. 7 (A) Nitrogen adsorption–desorption isotherms and (B) pore size distributions of the MCM-22 sample (M22_CS), ITQ-2 samples (IQ2_CS-10, IQ2_CS-45, IQ2_CS-90), and MCM-36 sample (M36_CS).

4. Catalytic properties of different MCM-22 samples for LAB synthesis

The catalytic performances of different MWW zeolites were tested during LAB synthesis using a benzene–dodecene mixture at a benzene/dodecene molar ratio of *x* (denoted as R*x* feed).

Fig. 8 depicts the catalytic performances of the three MCM-22 samples using R10 feed at a reaction temperature of

Table 2 Catalytic performances of various MWW samples during *n*-propylbenzene disproportionation

	M22_			IQ2_			
Sample ID	CS	ASp	AR	CS-10	CS-45	CS-90	M36_CS
Reaction conditions							
T (°C)	200	200	200	200	250	250	250
WHSV (h^{-1})	5	3	3	3	3	3	3
Conv. (wt%)	5.0	5.7	9.1	3.8	2.7	3.6	2.8
Reaction selectivity							
B/DPB (mol)	1.1	1.1	1.2	1.1	1.1	1.1	1.1
*ni*DPB (%)	48	37	37	48	48	33	36
*nn*DPB (%)	52	63	63	52	52	67	64
Product selectivity (%)							
C_6^- light gas	0.02	0.03	0.1	0.1	0.1	0.1	0.02
Benzene	1.5	1.7	3.1	1.1	0.7	1.1	0.8
n-PB	95.0	94.3	90.9	96.2	97.3	96.4	97.2
niPB	1.4	2.0	3.4	1.0	0.7	0.7	0.5
nnPB	1.5	1.2	2.0	1.1	0.7	1.4	0.9
Others	0.6	0.8	0.5	0.6	0.6	0.4	0.6

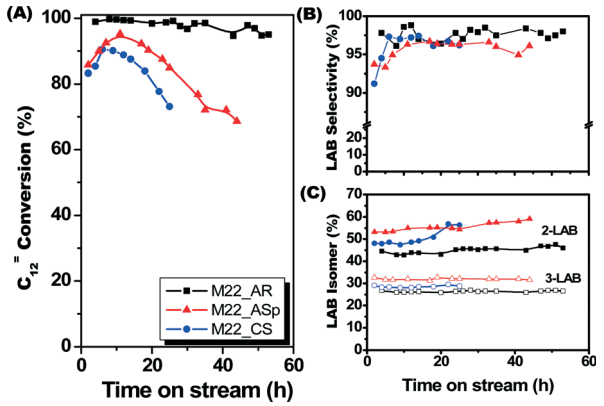

Fig. 8 (A) 1-Dodecene conversion, (B) LAB product selectivity, and (C) LAB isomer selectivity during LAB synthesis over different MCM-22 samples along with time-on-stream (reaction temperature: 433 K; pressure: 2068 kPa; WHSV: 4 h^{-1}; H_2/total HC molar ratio: 3.0; R10 feed composition: benzene/*n*-decane/1-dodecene = 10 : 0.5 : 1 mol mol^{-1}).

433 K. While M22_AR was catalytically stable reaching a dodecene conversion nearly 100%, M22_CS and M22_ASp were both deactivated along with increasing time-on-stream (TOS) (Fig. 8A). All the three MCM-22 samples catalysed nearly 100% LAB product selectivity with very low multi-alkylation side products (Fig. 8B). As for the LAB isomer selectivity, their 3-LAB isomer selectivities were about the same; however, M22_AR exhibited a 2-LAB isomer selectivity of 45% as the lowest one (Fig. 8C). The higher 2-LAB isomer selectivity over M22_ASp and M22_CS could be due to their 12-MR pore structure and also coke deposition on the 12-MR pore in the MWW zeolite that arose from deactivation. More discussion will be presented in the following sections.

When R4 feed was used, the M22_AR was catalytically unstable (Fig. 9A). Accordingly, catalyst deactivation was accelerated using benzene lean feed. During catalytic LAB synthesis, the catalytic stability ranked in the descending order of M22_AR > M22_ASp > M22_CS, which could be attributed to the number of external surface 12-MR cages. Furthermore, the most stable catalyst sample M22_AR was subjected to various stability tests. In response to variable reaction temperatures, the M22_AR catalyst exhibited stable conversion at a reaction temperature of 433 K, and it deactivated very fast at a low reaction temperature of 393 K (Fig. 9B), indicating loss of catalytic stability at low reaction temperature. On the other hand, while M22_AR gave stable activity at WHSV of 4 h^{-1}, at WHSV higher than 20 h^{-1} the catalyst was still active but seriously deactivated (Fig. 9C).

5. Catalytic behaviours of MWW zeolites

The catalytic performances of three ITQ-2 samples prepared from swollen M22_CS(P) by changing the delamination conditions were recorded. At a reaction temperature of 433 K using R10 feed, the three ITQ-2 samples all exhibited improved dodecene conversion and catalytic stability better than the M22_CS catalyst (Fig. 10A). The catalytic stability of the delaminated ITQ-2 sample becomes better with increasing ultrasonic delamination time from 10 min to 90 min. IQ2_CS-90 exhibited stable catalytic activity at high conversion and high LAB product selectivity (Fig. 10B). Notice that the mild and intermediate delaminated samples IQ2_CS-10 and IQ2_CS-45 exhibited slightly lower LAB product selectivity and tremendously higher dialkylate product selectivity (Table 3). Meanwhile, the three ITQ-2 catalysts all catalysed lower 2-LAB but high 6-LAB isomer selectivity than the other MWW zeolites (Fig. 10C and Table 3).

The catalytic stability of IQ2_CS-90 at increasing reaction severity was examined. As shown in Fig. 11, IQ2_CS-90 was stable using R10, R4 and even R2 feeds (traces a–c). For the octadiene doped R10 feed, IQ2_CS-90 remained catalytically stable being tolerant for octadiene impurity of 0.5% in the R10 feed (trace d05). By increasing the octadiene impurity beyond 1%, IQ2_CS-90 became unstable (trace d10).

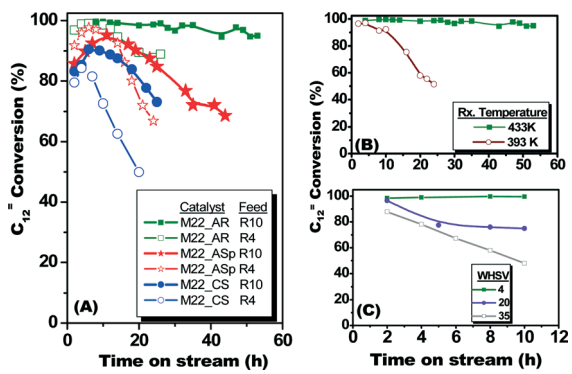

Fig. 9 Plot of 1-dodecene conversion along with time-on-stream in the case of (A) different MCM-22 samples in R10 and R4 feeds (reaction temperature: 433 K; pressure: 2068 kPa; WHSV: 4 h^{-1}; H_2/HC molar ratio: 3.0); (B) changing reaction temperature using R10 feed (reaction temperature: 393 and 433 K, other conditions were the same as (A)); and (C) changing weight hourly space velocity using R10 feed (WHSV: 4–35 h^{-1}, other conditions were the same as (A)).

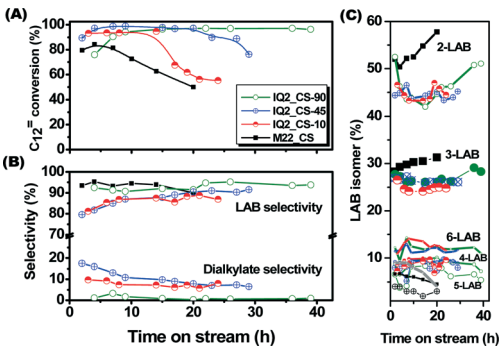

Fig. 10 (A) 1-Dodecene conversion, (B) LAB product selectivity, and (C) LAB isomer selectivity during LAB synthesis over MCM-22 and ITQ-2 catalysts along with time-on-stream (reaction temperature: 433 K; pressure: 2068 kPa; WHSV: 4 h^{-1}; H_2/HC molar ratio: 3.0; R4 feed composition: benzene/*n*-decane/1-dodecene = 4 : 0.5 : 1 mol mol^{-1}).

Table 3 Catalytic performances of MWW zeolites during LAB synthesis (reaction temperature: 433 K; pressure: 2068 kPa; WHSV: 4 h^{-1}; H_2/total HC molar ratio: 3.0)

Catalyst	M22_AR	M22_CS	M36_CS	IQ2_CS-10		IQ2_CS-45	IQ2_CS-90
Feed	R4	R4	R4	R4	R4	R4	R10DN.1
TOS (h)	10	2	24	14	20	26	27
$C_{12}^{=}$ (%)	98.5	79.5	96.6	94.6	97.2	97	50.9
Product selectivity (%)							
C_{10}–C_{12}	1.2	4.1	3.3	2.8	1.3	2.4	10.1
C_{12}–C_{18}	1.2	1.8	2.2	1.9	1.5	2.4	6.5
LAB	97.6	93.5	82.8	87.5	89.3	95.2	81.8
$>C_{18}$ dialkylate	0	0.6	11.7	7.8	7.9	0	1.6
LAB isomer selectivity (%)							
2-LAB	50.0	52.0	54.3	43.3	45.1	46.1	59.2
3-LAB	27.2	28.3	27.9	24.1	26.1	26.7	24.4
4-LAB	7.5	6.66	6.0	9.9	9.2	9.1	6.0
5-LAB	7.6	4	5.7	9.3	7.4	6.2	5.1
6-LAB	7.6	9	6.1	13.5	12.2	11.9	5.3

Meanwhile, the LAB product selectivity decreased (Fig. 11B) accompanied with increasing 2-LAB and decreasing 6-LAB isomer selectivity (Fig. 11C, Table 3). The light (C_{10}–C_{18}) hydrocarbons increased accordingly.

The catalytic performance of the pillared M36_CS sample was tested. During LAB synthesis using R10 and R4 feeds, among MWW zeolites, M36_CS and IQ2_CS-90 exhibited much more stable catalytic activity (Fig. 12, traces c–e) than M22_CS (traces a and b). Notice that M36_CS catalysed a lower LAB product selectivity with formation of more $>C_{18}$ di-alkylates (Table 3). With regard to LAB isomer selectivity, while M36_CS performance was similar to M22_CS, IQ2_CS-90 exhibited a lower 2-LAB selectivity and a higher 6-LAB selectivity. Therefore, the swollen MCM-22(P) precursor can subsequently be delaminated or pillared to produce ITQ-2 or MCM-36 with improved catalytic activity and stability for LAB synthesis application.

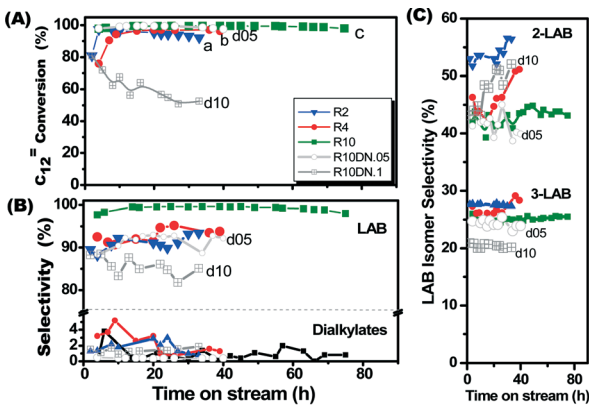

Fig. 11 (A) 1-Dodecene conversion, (B) LAB product selectivity, and (C) LAB isomer selectivity during LAB synthesis using various feeds with or without octadiene impurity over the IQ2_CS-90 catalyst along with time-on-stream (reaction temperature: 433 K; pressure: 2068 kPa; WHSV: 4 h^{-1}; H_2/total HC molar ratio: 3.0; composition: benzene/*n*-decane/1-dodecene/octadiene = *x* : 0.5 : 1 : 0 (0.05 or 0.1) mol mol^{-1}).

6. Impurity induced deactivation of MWW zeolites during LAB synthesis

Selective poisoning with collidine on the MWW zeolite during LAB synthesis was studied to identify the active sites of MWW zeolites. Octadiene was used as a model compound for the study on the effect of feed impurity on the catalytic performance of MWW zeolite.

Collidine having a large molecular size of 7.4 Å could be selectively adsorbed on the 12-MR pore of the MCM-22 zeolite.[26] Presumably, collidine would be selectively adsorbed on the external acid sites located in the isolated 12-MR cages on the external surface of the MWW zeolite without attacking the internal acid sites located in the internal supercage or in sinusoidal 10-MR pore channels. The effect of collidine poisoning on the catalytic performance of M22_CS was studied in a six-stage testing (Fig. 13). As shown in Fig. 13A-1, during stage (a) using normal R10 feed at a benzene/dodecene molar ratio of 10, M22_CS deactivated slightly giving 85% dodecene conversion and 95% LAB selectivity. During stage (b) after TOS of 8 h, while 0.5% collidine doped R10 was used as feed, M22_CS subjected to collidine poisoning was deactivated continuously showing a sharp drop in both dodecene conversion and LAB product selectivity accompanied by formation of more light (C_{10}–C_{18}) hydrocarbon by-products. During stage (c) after TOS of 13 h, the testing feed was changed to the normal collidine-free R10 feed; the reduction in dodecene conversion and LAB product selectivity became slower. During stage (d), the poisoned M22_CS was subjected to a hot stripping treatment to wash out/desorb collidine from the catalyst using pure benzene at 400 °C for 6 h. Stage (e) started another testing with normal R10 feed; the treated M22_CS exhibited a similar catalytic performance as stage (a). During stage (f) after TOS of 34 h, serious catalyst deactivation resulting from using 0.5% collidine doped R10 feed led to a dramatic reduction in dodecene conversion and much more deteriorated LAB product selectivity.

As shown in Fig. 13B-1, IQ2_CS-90 was tested following the same testing sequence stated above for M22_CS. During

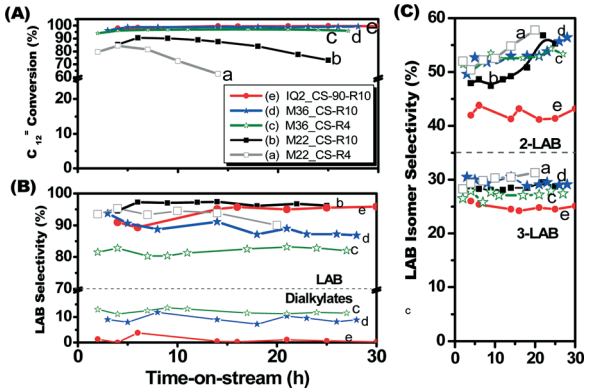

Fig. 12 (A) 1-Dodecene conversion, (B) LAB product selectivity, and (C) LAB isomer selectivity during LAB synthesis using R4 and R10 feeds over different MWW zeolites along with time-on-stream (reaction temperature: 433 K; pressure: 2068 kPa; WHSV: 4 h^{-1}; H_2/total HC molar ratio: 3.0).

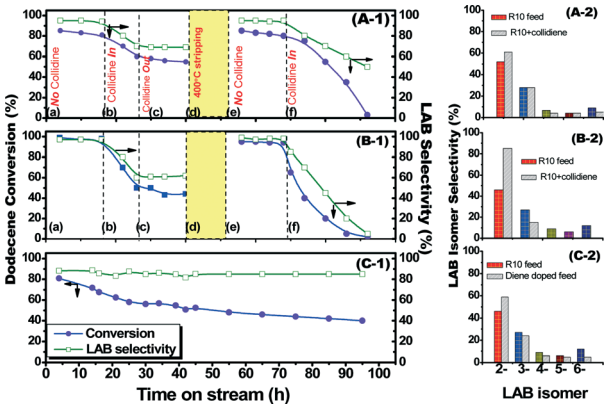

Fig. 13 Monitoring of catalytic performance of M22_AR (A-1 and A-2) and IQ2_CS-90 (B-1 and B-2) during a six-stage operation for LAB synthesis using collidine doped R10 feed and IQ2_CS-90 using octadiene doped R10 feed (C-1 and C-2) (R10 feed; reaction temperature: 433 K; pressure: 2068 kPa; WHSV: 4 h^{-1}; H_2/HC molar ratio: 3.0). During the six-stage operation: reaction (a) using normal feed, (b) using 0.5% collidine doped feed, (c) using feed, and (d) 673 K stripping with benzene feed and then reaction (e) using normal feed and (f) using 0.5% collidine doped feed.

stage (a), IQ2_CS was more catalytic stable than M22_CS. While IQ2_CS-90 and M22_CS exhibited a similar collidine effect leading to fast deactivation and reduced dodecene conversion, IQ2_CS exhibited a much more pronounced effect with a much worse LAB product selectivity.

On the other hand, the deactivation behaviour of IQ2_CS-90 in using octadiene doped R10 feed was monitored (Fig. 13C-1). Along with increasing TOS, dodecene conversion decreased as an indication of serious catalyst deactivation, and LAB product selectivity remained relatively constant.

In the A-1, B-1 and C-1 tests, those catalysts after deactivation either by collidine selective adsorption or octadiene contamination all exhibited higher 2-LAB selectivity and reduced 6-LAB isomer selectivity (Fig. 13A-2, B-2, and C-2). The change in LAB isomer selectivity was particularly evident for the collidine poisoning on the ITQ-2 catalyst (Fig. 13B), which might be attributed to the pore structure effect.

Discussion

MWW zeolites have three pore systems, namely, a sinusoidal 10-MR pore channel with an aperture of 0.4 × 0.59 nm, a 10-MR interconnected supercage of 1.8 × 0.7 nm, and an external surface 12-MR cage having an aperture of approximately 0.7 nm and a longitude length of 0.7 nm.[12] For convenience, the three pore systems located with acid sites are denoted as S_R10-10 in the R10-10 micropore, the S_C10-12 site in supercage C10-12, and the S_EC12 site in external cage EC-12.

As shown in Table 1, the S_{meso} and V_{meso} of the three MCM-22 samples varied from each other, which could be attributed to their crystal morphology. On the other hand, all the ITQ-2 and MCM-36 samples had much larger S_{meso} and V_{meso} than the MCM-22 samples, indicating that the delamination or pillaring method could increase the S_{meso} and V_{meso} of MCM-22 more effectively than the morphology-induced enhancement in the MCM-22 sample.

Taking the advantage of the effect of the disproportionation mechanism, *n*-PB disproportionation could be used to differentiate the 10-MR micropore from the 12-MR micropore in MWW zeolite samples by examining *nn*DPB isomer selectivity. The S_{meso} determined from the nitrogen sorption isotherm and *nn*DPB isomer selectivity during the *n*-PB disproportionation ranked in the same order as ITQ-2 > MCM-36 > MCM-22. As shown in Table 2, among the three MCM-22 samples, M22_CS catalysed higher *ni*DPB and lower *nn*DPB product selectivity. Presumably, M22_CS forming as stacks of the large crystal had the lowest number of external surface cage EC-12. On the other hand, M22_AR with the smallest crystal size possessed the highest number of EC-12 and S_{meso}. Accordingly, increasing S_{meso} arise mainly from more surface cage EC-12, not just from the contribution of the intercrystalline non-framework voidage from the small crystal.

On the other hand, IQ2_CS-90 and M36_CS catalysed higher *nn*DPB than M22_CS did. Since ITQ-2 is prepared from MCM-22(P) by delamination, ITQ-2 should increase profoundly the number of surface cage EC-12. On the other hand, MCM-36 by pillaring has increased the C10-12 supercage at increasing longitude length and mesopore volume, while the micropore volume could be reduced due to silica blocking partially on the 10-MR pore R10_10.[13,27] The extent of silica blocking on MCM-36 would depend on the pillaring protocol.

While most of the 12-MR zeolites are catalytically active for LAB synthesis, 8-MR and 10-MR zeolites are inactive. Presumably, limited by the available space for LAB molecules, the S_R10-10 (sinusoidal 10-MR site) of the MWW zeolite is catalytically inactive. Therefore, the active sites could be attributed to the acid sites located in supercage C10-12 (S_C10-12) and on the external cage (S_EC12). As noted above, the M22_AR and M22_CS samples contained the 10-MR zeolite impurity phase. Nevertheless, they had similar high dodecene

conversion. Particularly, M22_AR exhibited excellent catalytic stability. Presumably, the 10-MR zeolite was inactive in LAB synthesis, and the 10-MR zeolite impurity phase had a very minor effect on the catalytic stability of MWW zeolites.

In pillared MCM-36, the pore volume of the C10-12 supercage increases without too much modification on its 10-MR pore aperture and the surface cage EC-12. As shown in Fig. 12 and Table 3, M36_CS exhibited high catalytic activity with a much higher di-alkylate product selectivity than other MWW zeolites. Clearly, the acid site (S_C10-12) located in the C10-12 supercage predominates LAB synthesis. The enlarged pore volume of the C10-12 supercage of M36_CS after pillaring allows the active site S_C10-12 to catalyse more multi-alkylation, resulting in increased di-alkylate product formation in the compensation of mono-alkylate selectivity. Meanwhile, because the 10-MR aperture of the C10-12 supercage remained practically the same, M36_CS catalysed the same LAB isomer product distribution as M22_CS.

Delamination of MCM-22 platelet crystals could open up most of C10-12 supercages through which a great number of additional surface cages EC-12 are generated. Therefore, ITQ-2 possesses excessive external surface area and EC-12 sites. Notice that during LAB synthesis all three ITQ-2 samples catalysed higher 4- and 6-LAB isomer selectivities in compensation of the lower 2-LAB isomer selectivity (Table 3 and Fig. 10). Generally speaking, 2-LAB isomer selectivity increases with decreasing aperture of the zeolite micropore.[1] The lowest 2-LAB isomer selectivity among MWW zeolites indicates that the predominant active site of ITQ-2 for LAB synthesis is located at surface cage EC-12 with a larger aperture of 0.7 nm leaving the less active site located at supercage C10-12 with an aperture of 0.59 nm. On the other hand, the predominant active sites of MCM-36 are located at supercage C10-12.

A different deactivation behaviour was observed when the impurity of feed and MWW structure were changed (Fig. 13). Upon collidine poisoning, IQ2_CS-90 deactivated much faster than M22_CS (Fig. 13 B-1 *vs.* A-1). Those selective poisoning tests further indicate that LAB synthesis is catalysed predominantly by the active site S_EC-12 located on the surface 12-MR cage. According to Du and Olson,[20] collidine can selectively poison the Brønsted acid sites S_EC-12 on the MWW surface without influencing the access to intracrystalline acid sites S_C10-12. As a result, the non-poisoned S_C10-12 site and the 10-MR site S_R10-10 remained active for the non-selective catalysis for by-product formation such as cracking and short chain alkylation of benzene, leading to reduced LAB product selectivity. Since the predominant active sites of IQ2_CS-90 was S_EC-12, therefore its deactivation rate upon collidine poisoning was much worse than MCM-22.

On the other hand, non-selective deactivation by octadiene containing the R10 feed leading to un-changed LAB product selectivity along the deactivation course was observed (Fig. 13C-1). In the case of octadiene deactivation, octadiene could react non-selectively at all the three active sites located inside the 10-MR and 12-MR pores in the MWW zeolites, leading to uniform catalyst deactivation. Accordingly, during the deactivation course, coke precursors built up inside the micropore which induced the shape selective formation of 2-LAB with un-changed LAB product selectivity. As shown in Fig. 13A-2, B-2, C-2, deactivation originated from either collidine poisoning or octadiene contamination leading to increasing 2-LAB with decreasing 6-LAB isomer selectivity.

ITQ-2 by delamination exhibited profound catalytic stability. By increasing delamination time, during *n*-PB disproportionation the ITQ-2 catalyzes higher *nn*DPB (Table 2), and ITQ-2 becomes more catalytic stable during LAB synthesis (Fig. 10). Increasing the number of EC-12 surface cages by delamination along with increasing S_{meso} and V_{meso} could substantially improve the catalytic stability. IQ2_CS-90 could even be stable in the octadiene containing feed (Fig. 11).

Among the three MCM-22 samples, M22_AR having the highest *nn*DPB selectivity during *n*-PB disproportionation exhibited improved catalytic stability better than M22_ASp and M22_CS. Presumably, M22_AR had more S_EC12 sites on the surface cage EC-12, which imposed the least resistance for product diffusion. On the other hand, M22_CS with the regular stacking of large platelets opened up less surface cages. Therefore, M22_CS handicapped with stronger diffusion resistance showed the poorest catalytic stability.

Alternatively, the pillared MCM-36 showed much improved catalytic stability in comparison to MCM-22. A supercage that usually has a strong coking tendency, such as the FAU zeolite, is often harmful to catalytic stability. In the case of MWW zeolite, the extraordinarily large supercage C10-12 in MCM-36 does provide improved diffusivity and catalytic stability. Lin *et al.* reported that the catalytic stability of mordenite for LAB synthesis could be improved by introduction of mesoporosity with a wide pore size distribution.[5] MWW zeolites provide another approach for hybrid micro–meso interconnecting pore systems.

Conclusions

The catalytic performances of different MWW zeolites were studied for LAB synthesis using a benzene–dodecene mixture at various compositions. It was found that their micro–meso hierarchical porosity plays a major role in controlling the catalytic stability and LAB isomer selectivity. In association with characterization of textural properties, catalytic tests including selective collidine poisoning, octadiene deactivation tests and *n*-propylbenzene disproportionation were conducted to identify the location of the active site for LAB synthesis. Apparently, the acid sites located on the external surface 12-oxygen membered ring (12-MR) cage (EC-12) and the internal 10-MR interconnected with 12-MR (C10-12) supercages in MWW zeolites were identified as the active sites for LAB synthesis.

In reference to the catalytic testing results, most of the mesoporous surface areas (S_{meso}) of the MWW zeolites come from the surface cage EC-12 and internal supercage C10-12. The catalytic stability of MCM-22 obtained from the optimum

preparation protocol could be improved by increasing the number of EC-12 cages as well as increasing the S_{meso} and pore volume. Furthermore, delamination or pillaring of the swollen MCM-22(P) precursor to prepare ITQ-2 or MCM-36 zeolite, respectively, could further improve the catalytic stability for LAB synthesis.

By delamination, the ITQ-2 zeolite creates more surface cage EC-12 and S_{meso}. The catalytic activity of ITQ-2 for the LAB synthesis comes mainly from the acid site located at surface cage EC-12 with a larger aperture of 0.7 nm outweighing the acid site located at supercage C10-12 with an aperture of 0.59 nm. Extending delamination treating time could increase the number of EC-12 surface cages and thus improve the catalytic stability of ITQ-2 with reduced 2-phenyl LAB isomer selectivity. An optimum ITQ-2 sample subjected to delamination for 90 min exhibited strong stability even in benzene lean LAB feed or 0.1% octadiene-containing feed.

The pillared MCM-36 zeolite increases the C10-12 supercage and S_{meso}, enabling MCM-36 to catalyse a lower LAB product selectivity with formation of more di-alkylate by-products with a similar LAB isomer selectivity.

Acknowledgements

We acknowledge the Sinopec Research Institute of Petroleum Processing for providing the zeolite sample. This study was financially supported by the Ministry of Science and Technology of R.O.C. (MOST 102-2622-E-390-001-CC1).

References

1 A. Aitani, J. B. Wang, I. Wang, S. Al-Khattaf and T. C. Tsai, *Catal. Surv. Asia*, 2014, **18**, 1.
2 S. Sivasanker and A. Thangaraj, *J. Catal.*, 1992, **138**, 386.
3 S. V. Awate, S. B. Waghmode and M. S. Agashe, *Catal. Commun.*, 2004, **5**, 407.
4 J. Kocal, B. Vora and T. Imai, *Appl. Catal., A*, 2001, **221**, 295.
5 J. S. Lin, J. J. Wang, J. Wang, I. Wang, R. J. Balasamy, A. Aitani, S. Al-Khattaf and T. C. Tsai, *J. Catal.*, 2013, **300**, 81.
6 V. Valtchev, G. Majano, S. Mintova and J. Pérez-Ramírez, *Chem. Soc. Rev.*, 2013, **42**, 263.
7 P. Meriaudeau, Y. B. Taarit, A. Thangaraj, J. L. G. Almeida and C. Naccache, *Catal. Today*, 1997, **38**, 243.
8 M. H. Han, Z. Cui, C. Xu, W. Chen and Y. Jin, *Appl. Catal., A*, 2003, **238**, 99.
9 Y. Cao, R. Kessas, C. Naccache and Y. B. Taarit, *Appl. Catal., A*, 1999, **184**, 231.
10 M. Mazur, P. Chlubná-Eliášová, W. J. Roth and J. Cějka, *Catal. Today*, 2014, **227**, 37.
11 M. E. Leonowicz, J. A. Lawton, S. L. Lawton and M. K. Rubin, *Science*, 1994, **264**, 1910.
12 A. Corma, V. Fornes, S. Pergher, T. L. Maesen and J. Buglass, *Nature*, 1998, **396**, 353.
13 W. J. Roth, C. T. Kresge, J. C. Vartuli, M. E. Leonowicz, A. S. Fung and S. B. Mccullen, *Stud. Surf. Sci. Catal.*, 1995, **94**, 301.
14 S. Maheshwari, E. Jordan, S. Kumar, F. S. Bates, R. L. Penn, D. F. Shantz and M. Tsapatsis, *J. Am. Chem. Soc.*, 2008, **130**, 1507.
15 W. J. Roth, W. Makowski, B. Marszalek, P. Michorczyk, W. Skuzaa and B. Gil, *J. Mater. Chem. A*, 2014, **2**, 15722.
16 P. Wu, J. F. Ruan, L. L. Wang, L. L. Wu, Y. Wang, Y. M. Liu, W. B. Fan, M. Y. He, O. Terasaki and T. Tatsumi, *J. Am. Chem. Soc.*, 2008, **130**, 8178.
17 A. Corma, V. Martınez-Soria and E. Schnoeveld, *J. Catal.*, 2000, **192**, 163.
18 C. C. Tsai, C. Y. Zhong, I. Wang, S. B. Liu, W. H. Chen and T. C. Tsai, *Appl. Catal., A*, 2004, **267**, 87.
19 Y. J. Ji, B. Zhang, L. Xu, H. Wu, H. Peng, L. Chen, Y. Liu and P. Wu, *J. Catal.*, 2011, **283**, 168.
20 H. Du and D. H. Olson, *J. Phys. Chem. B*, 2002, **106**, 395.
21 H. K. Min, M. B. Park and S. B. Hong, *J. Catal.*, 2010, **271**, 186.
22 A. Corma, C. Corell and J. Perez-Pariente, *Zeolites*, 1995, **15**, 655.
23 Z. Liu, Z. Fu, M. He, M. Lee and B. Zong, CN1353010A, 2002.
24 A. Corma, V. Fornes, J. M. Guil, S. Pergher, Th. L. M. Maesen and J. G. Buglass, *Microporous Mesoporous Mater.*, 2000, **38**, 301.
25 T. C. Tsai and I. Wang, *J. Catal.*, 1992, **133**, 136.
26 F. Thibault-Starzyk, I. Stan, S. Abelló, A. Bonilla, K. Thomas, C. Fernandez, J.-P. Gilson and J. Pérez-Ramírez, *J. Catal.*, 2009, **264**, 11.
27 A. Corma, V. Fornes, J. Martínez-Triguero and S. B. Pergher, *J. Catal.*, 1999, **186**, 57.

